Sensors & Actuators: B. Chemical 436 (2025) 137687

Contents lists available at ScienceDirect

Sensors and Actuators: B. Chemical

journal homepage: www.elsevier.com/locate/snb

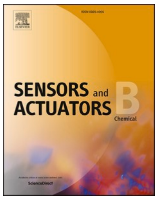

Low-triggered-potential electrochemiluminescence platform based on anodic-emitting Yb-MOF for sensitive detection of APE1

Ruiyan Liu [a], Yike Xu [b], Zhuoxin Ye [a], Yuxuan Chen [a], Yan Zhang [a], Mo Ma [a,c], Pinyi Ma [a,*], Qiong Wu [b,*], Daqian Song [a,*]

[a] *College of Chemistry, Jilin Province Research Center for Engineering and Technology of Spectral Analytical Instruments, Jilin University, Qianjin Street 2699, Changchun 130012, China*

[b] *Key Laboratory of Pathobiology, Ministry of Education, Nanomedicine and Translational Research Center, The Third Bethune Hospital of Jilin University, Sendai Street 126, Changchun 130033, China*

[c] *School of Pharmacy, Jilin University, Qianjin Street 2699, Changchun 130012, China*

ARTICLE INFO

Keywords:
Metal-organic framework (MOF)
Electrochemiluminescence (ECL)
Low triggering potential
Biosensor
Apurinic/apyrimidinic endonuclease 1 (APE1)

ABSTRACT

Porphyrins possess excellent electrochemiluminescence (ECL) properties but suffer from aggregation-induced quenching (ACQ) in aqueous solutions. Metal-organic frameworks (MOFs) can effectively mitigate this issue by restricting porphyrin aggregation. However, existing studies predominantly focus on cathodic ECL emission at highly negative trigger potentials, which often leads to undesirable hydrogen evolution side reactions. To overcome this challenge, we developed a novel Yb-based MOF (Yb-TCPP) with anodic ECL emission and a low triggering potential. Yb-TCPP was synthesized via the hydrothermal reaction, using 5,10,15,20-tetra(4-carboxyphenyl)-porphyrin (H_2TCPP) as the organic linker. Among a series of Yb-MOFs (Yb-ETTC, Yb-CTTB, Yb-BCPP), Yb-TCPP had the strongest ECL emission, with an intensity reaching ~ 11000 a.u. Further modification with gold nanoparticles (AuNPs) significantly enhanced its conductivity and ECL performance. The resulting Yb-TCPP@AuNPs exhibited a low triggering potential of + 0.47 V, effectively avoiding oxygen evolution side reactions. With the Φ_{ECL} of $[Ru(bpy)_3]^{2+}$/triethylamine (TEA) set as 1, it also achieved a high ECL efficiency (Φ_{ECL}) of 11 %. These results highlight the potential of Yb-TCPP@AuNPs as a robust anodic ECL material for biosensing applications. Based on this material, we constructed an "on-off" ECL biosensor for the sensitive detection of apurinic/apyrimidinic endonuclease 1 (APE1) using catalytic hairpin amplification (CHA). The sensor had a linear detection range of 1×10^{-8} U/mL to 1×10^{-2} U/mL and a detection limit of 1.58×10^{-9} U/mL. In summary, this study presents the successful development of Yb-TCPP@AuNPs as a promising anodic ECL platform, providing new insights into the development of advanced ECL materials for clinical diagnostics.

1. Introduction

Electrochemiluminescence (ECL) combines the advantages of electrochemistry and chemiluminescence to provide high sensitivity and specificity, which makes it a tool widely used in optoelectronic and biosensing applications [1]. Existing ECL materials include inorganic [2,3], organic [4,5] and nano-luminescent materials [6,7]. Among these materials, organic luminescent materials have gained the most attention due to their structural adaptability, modifiability, biocompatibility, and excellent optoelectronic properties. However, most polycyclic aromatic hydrocarbons (PAHs) suffer from aggregation-caused quenching (ACQ), and thus their luminescent performance in aqueous solutions is low [8–10]. Metal-organic frameworks (MOFs) can effectively address this limitation by restricting PAH aggregation through their porous structures and enhancing electron-hole recombination efficiency [11,12]. For example, Cui's group developed Zn-TCPP/UiO-66-NH_2, which is a MOF based on 5,10,15,20-tetra(4-carboxyphenyl)-porphyrin (H_2TCPP), to mitigate the ACQ effect. Despite these advancements, ECL emission of Zn-TCPP is primarily limited to cathodic processes at extremely negative potentials (-2 V), which in turn leads to undesirable hydrogen evolution side reactions that can compromise biological activity [13]. Anodic ECL emission offers a compelling alternative due to its lower triggering potential and reduced electrochemical interference. Rare earth MOFs have gained considerable attention for their active sites, photoelectric

---

* Corresponding authors.
E-mail addresses: mapinyi@jlu.edu.cn (P. Ma), qiong_wu@jlu.edu.cn (Q. Wu), songdq@jlu.edu.cn (D. Song).

https://doi.org/10.1016/j.snb.2025.137687
Received 1 February 2025; Received in revised form 15 March 2025; Accepted 23 March 2025

properties, and stability [14–16]. Wei's group have reported Ce-MOF with excellent ECL stability (RSD of 0.77 %) [17]. Building on these findings, we developed a Yb-based MOF (Yb-TCPP) as an anodic ECL emitter that not only can mitigate the ACQ effect of H_2TCPP but also can provide strong and stable anodic ECL emission at low triggering potentials.

Apurinic/apyrimidinic endonuclease 1 (APE1) is a key enzyme in the base excision repair (BER) pathway responsible for cleaving phosphodiester bonds at apurinic/apyrimidinic (AP) sites [18]. APE1 is associated with various diseases, including cancer and neurodegenerative disorders, and has elevated expression in multiple cancers such as breast, lung, bladder, and pancreatic cancer [19,20]. Current methods for APE1 detection, including liquid chromatography and fluorescent biosensors, are time-consuming and have low sensitivity [21,22]. With ultra-high sensitivity and rapid detection capabilities, ECL technology presents a promising solution for APE1 detection.

In this work, a novel ECL biosensor was constructed for the sensitive detection of APE1 using Yb-TCPP modified with gold nanoparticles (AuNPs) as anodic ECL emitters, in combination with catalytic hairpin amplification (CHA). We successfully synthesized Yb-TCPP through the hydrothermal reaction (Scheme A). Due to its large surface area, high porosity, and rich three-dimensional spatial structure, Yb-TCPP was able to reduce the ACQ effect of H_2TCPP and improve the electron-hole recombination efficiency. Due to the poor electrical conductivity of MOF, it has been shown that modifying its surface with metal particles by post-synthetic modification (PSM) can increase its electrical conductivity [23,24]. Therefore, we successfully synthesized Yb-TCPP@AuNPs through PSM to enhance both its electrical conductivity and ECL intensity. Furthermore, in Scheme B, we obtained S2, which could drive the CHA process (Scheme C) by reacting the target APE1 with the hairpin R1 modified at the AP site. In Scheme C, the CHA process was introduced, where S2 sequentially opened the hairpin H1, H2, and H3 to ultimately obtain the Y-shaped DNA structure while releasing S2. Among them, H2 was modified with sulfhydryl groups, which could bind to AuNPs through an Au-S bond (Scheme D). Then, the Y-shaped DNA structure captured R2 containing ferrocene, resulting in signal quenching. In the presence of APE1, the above processes occurred, causing the signal to be in the "off" state (details are shown in Supplementary Material under polyacrylamide gel electrophoresis analysis of CHA and Fig. S1). This detection method is highly sensitive and provides a new idea for the early diagnosis of APE1-associated cancers.

2. Experimental section

2.1. Synthesis of Yb-MOFs

Yb-TCPP was synthesized using the solvothermal method with minor modifications [25]. First, 11.7 mg of Yb $(NO_3)_3{\cdot}5\ H_2O$, 10 mg of H_2TCPP, and 0.5 mL of acetic acid were dissolved in 10 mL of DMF and the mixture was ultrasonicated for 5 min. Then the mixture was transferred into a Teflon cylinder, which was then placed in an oven at 120°C for 12 h. After heating, the product was washed twice with DMF, followed by ethanol, and then centrifuged at 8000 rpm for 10 min. After centrifugation, the products were dried in a vacuum oven at room temperature. Other Yb-TCPPs were also prepared by adjusting the dosage of Yb $(NO_3)_3{\cdot}5\ H_2O$ to 11.7 mg, 23.4 mg, 29.19 mg, and 35.03 mg.

Yb-CTTB, Yb-ETTC, and Yb-BCPP were synthesized using the same method described above, but with H_4CTTB, H_4ETTC, and H_4BCPP of 8.4 mg, 10.6 mg, and 11.2 mg, respectively.

2.2. Synthesis of Yb-TCPP@AuNPs

Yb-TCPP@AuNPs were synthesized by PSM [26]. Firstly, 3 mg of Yb-TCPP was dispersed in 3 mL of deionized water and mixed thoroughly using ultrasound. While stirring vigorously, $HAuCl_4$ (20 μL, 10 mM) was added to a sealed vial, and the mixture was stirred in the dark for 2 h. Then, the sediment was collected by centrifugation (8000 rpm, 15 min) and washed twice with deionized water. After that, the precipitate was dispersed in 3 mL of deionized water, and the freshly prepared $NaBH_4$ (0.1 mol/L, 3 μL) was quickly injected into the vial and stirred vigorously for 30 min. The product was then washed twice with deionized water and centrifuged (8000 rpm, 15 min). Following centrifugation, the product was dried in a vacuum drying oven at room temperature.

2.3. Assembly of Y-shaped DNA structures

First, R1, H1, H2, and H3 were heated to 95°C for 10 min. After slowly cooling to 25℃, they were annealed to form a hairpin structure. R1 was mixed with different concentrations of APE1 for 1 h at 37°C. Then, the mixture was heated at 65°C for 20 min to inactivate APE1. The Y-shaped DNA structure was obtained by mixing the inactivated product with H1, H2, and H3 (final concentration = 0.2 μM) and incubating at 37°C for 2 h.

2.4. Measurement procedure and proposed biosensor

First, the bare glassy carbon electrode (GCE) was polished with 0.3 μm and 0.05 μm aluminum powder and then ultrasonicated in high-purity water and ethanol to obtain a clean electrode surface. Then, 10 μL of 0.1 mg/mL Yb-TCPP@AuNPs solution was dropped onto the electrode surface and dried at 37°C to obtain Yb-TCPP@AuNPs/GCE. Next, Y/Yb-TCPP@AuNPs/GCE was formed by dropping 10 μL of sulfhydryl group-modified Y-shaped structure (previously treated with TCEP) onto Yb-TCPP@AuNPs/GCE and incubating overnight at room temperature. Subsequently, 10 μL of 1 μM hexyl mercaptan (HT) was dropped onto Y/Yb-TCPP@AuNPs/GCE and incubated at 37°C for 40 min to block the specific binding site. Ferrocene-modified R2 (1 μM) was then dropped onto HT/Y/Yb-TCPP@AuNPs/GCE to hybridize with Y to achieve signal quenching. After each of these steps, the electrode was washed with ultra-pure water. The ECL signal was measured in a triethylamine (TEA) system (2 mL 0.1 M phosphate buffer saline (PBS) solution containing 35 mM TEA) using an MPI-ECL analyzer. The photomultiplier (PMT) was set to a high voltage of 650 V and a potential range of −1 V to + 0.65 V. The amplification series was set at 4.

3. Results and discussion

3.1. Characterization of Yb-TCPP and Yb-TCPP@AuNPs

We characterized the appearance of Yb-MOF using scanning electron microscopy (SEM) and transmission electron microscopy (TEM), as shown in Figs. 1A and S2. From these figures, the three-dimensional cube structure of Yb-TCPP obtained through a hydrothermal synthesis process could be observed. As the Yb content increased, the shape of Yb-TCPP changed. When the molar ratio of Yb:H_2TCPP was 4:1, the shape of Yb-TCPP (4:1) was regular and uniform. Yb-BCPP, Yb-CTTB, and Yb-ETTC exhibited different morphologies and structures, appearing as spheres, flower clusters, and needles, respectively (Fig. S3). As shown in Fig. 1B, the surface of Yb-TCPP was smooth with clear edges, while that of Yb-TCPP@AuNPs (Fig. 1C) was rough. Additionally, the modified AuNPs could be observed on the surface of Yb-TCPP, which firmly confirms that AuNPs were successfully modified on the surface of Yb-TCPP via PSM without affecting its surface morphology. The SEM mapping (Fig. 1D) indicated that C, N, O, Yb, and Au elements were uniformly distributed, further confirming that AuNPs were successfully modified on the surface of Yb-TCPP.

The Fourier transform infrared spectroscopy (FTIR) of Yb-TCPP (Fig. S4) showed the asymmetric stretching vibration peaks of C═O which belongs to H_2TCPP ligands at 1688 cm^{-1} and 1604 cm^{-1} were

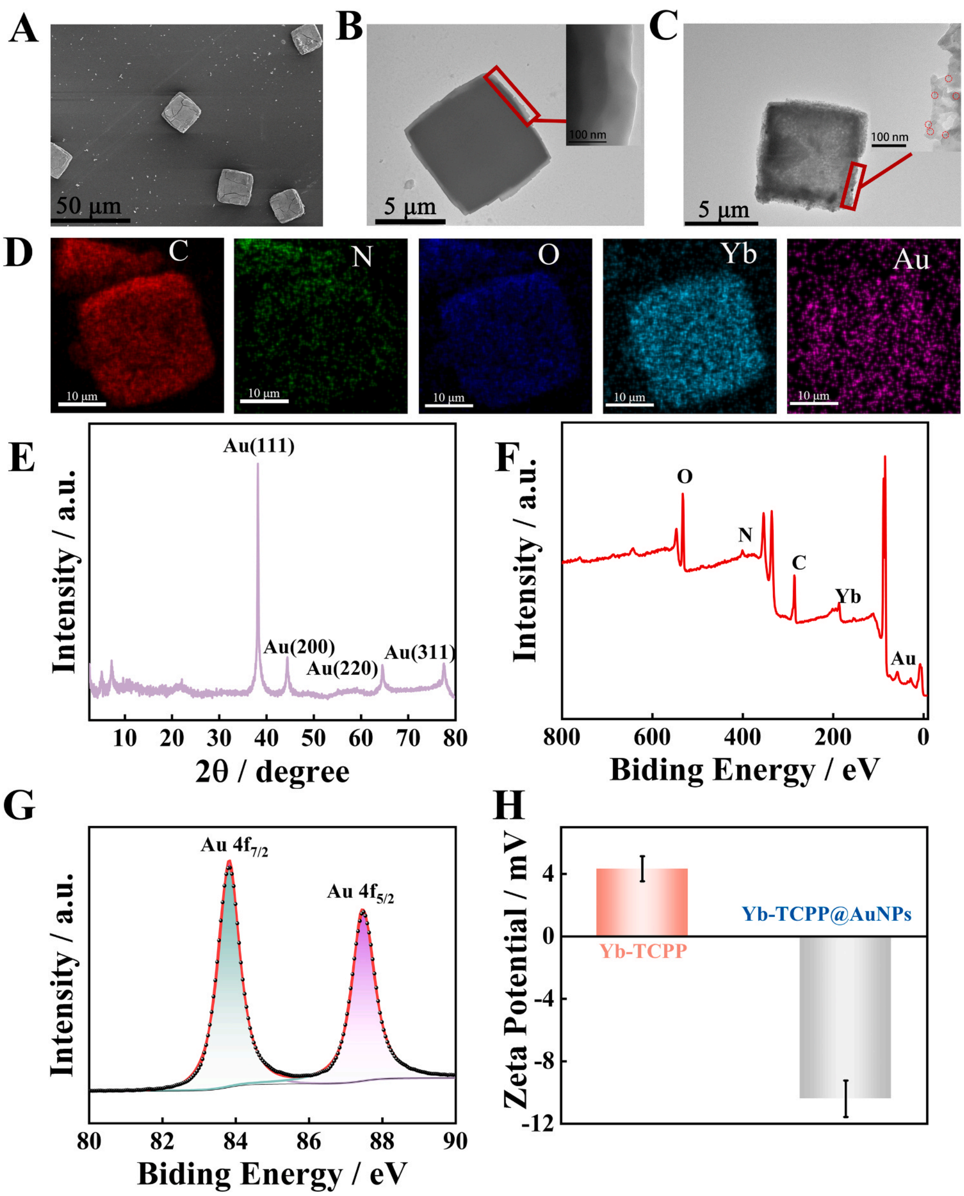

Fig. 1. (A) SEM images of three-dimensional Yb-TCPP (4:1) at 50-µm scale. (B) TEM images of three-dimensional Yb-TCPP (4:1) at 5-µm scale. (C) TEM images of Yb-TCPP@AuNPs at 5-µm scale. (D) SEM element mapping images of C, O, N, Yb, and Au elements. (E) XRD patterns of Yb-TCPP@AuNPs. (F) XPS spectra of Yb-TCPP@AuNPs. (G) Au 4 $f_{7/2}$ and 4 $f_{5/2}$ XPS spectra of Yb-TCPP@AuNPs. (H) Zeta potential of Yb-TCPP and Yb-TCPP@AuNPs.

shifted to 1603 cm^{-1} and 1531 cm^{-1}, respectively, and their intensities also decreased. Additionally, in the Yb-TCPP FTIR spectra, the C-O stretching vibration peak at 1277 cm^{-1} disappeared. The FTIR spectra of Yb-BCPP, Yb-CTTB, and Yb-ETTC were consistent with those of Yb-TCPP. This is in agreement with the literature [27], which has described that there is a strong coordination between Yb^{3+} and the carboxyl group in the ligand.

According to the X-ray diffraction pattern (XRD) of Yb-TCPP@AuNPs (Fig. 1E), it could be observed that the main diffraction peaks were consistent with those of Yb-TCPP (Fig. S5) in the low angle range of 2.5° to 30°. The appearance of several sets of diffraction peaks in the range of 30° to 80° indicated that AuNPs were successfully modified on the surface of Yb-TCPP. The strong diffraction peaks around 38.2°, 44.5°, 64.6° and 77.6° in the XRD pattern corresponded to Au (111), Au (200), Au (220), and Au (311), respectively [28]. The above results indicate that AuNPs did not alter the structure of Yb-TCPP. The XRD patterns (Fig. S5) of Yb-BCPP, Yb-CTTB, and Yb-ETTC were similar to those reported in the literature [29–31]. Furthermore, the X-ray photoelectron spectroscopic (XPS) results of Yb-TCPP@AuNPs showed the presence of O 1 s, C 1 s, N 1 s, Yb 4d, and Au 4 f (Fig. 1F and Fig. S6), confirming the successful synthesis of Yb-TCPP@AuNPs. In the high-resolution XPS of Au 4 f (Fig. 1G), there were two peaks at 83.85 eV and 87.5 eV, corresponding to Au 4 $f_{7/2}$ and Au 4 $f_{5/2}$, respectively. These peaks indicate that sodium borohydride could successfully reduce chloroauric acid. In surface zeta potential analysis (Fig. 1H), Yb-TCPP was positively charged, and after modification with AuNPs, the overall charge became negative [32]. The change in electrical charge indicates the AuNPs were successfully modified on the surface of Yb-TCPP via PSM. Additionally, we investigated the optical properties of the Yb-TCPP@AuNPs, including UV–vis absorption and fluorescence emission (Fig. S7 and Fig. S8).

3.2. ECL properties of Yb-TCPP@AuNPs

We investigated the ECL properties of Yb-TCPP and Yb-TCPP@AuNPs. The ECL properties of Yb-TCPP depend on the entry of the active TEA intermediates, which is influenced by the shape and size of the MOF [33]. Therefore, the ECL intensities of the MOFs synthesized from varying ratios of Yb^{3+} and H_2TCPP were different. Among them, Yb-TCPP (4:1) had a uniform and regular shape, which resulted in the strongest ECL intensity, about 11,000 a.u. (Fig. 2A). Furthermore, we synthesized three other types of Yb-MOFs with different PAHs based on the optimal ratio and investigated their ECL properties at the anode. As shown in Fig. 2B, in the same voltage range, the ECL intensity of Yb-TCPP was the strongest, while that of Yb-CTTB and Yb-BCPP were the weakest. Therefore, we may conclude that Yb-TCPP has excellent anode ECL emission. In order to gain an in-depth understanding of the differences in the ECL performance of these aromatic ligands, we obtained the molecular orbitals iso-surface plots and energy levels of the Yb-MOF leading orbitals using the Gaussian B3LYP function and 6–31 G (d, p) basis. As can be seen in Fig. 2C, the electron densities of the four Yb-based MOFs were delocalized over the entire molecule. As is well-known, bandgap is a key property that determines electrical and optical properties in materials [34,35]. And the HOMO-LUMO energy gap and electronic interaction between organic linkers determine the feasibility of electron withdrawal and donation [36]. ECL emission occurs when the excited state relaxes back to the ground state. The smaller HOMO-LUMO gap generally results in stronger emission, raising the possibility of emitting photons. The energy gaps of the HOMO-LUMO of Yb-TCPP, Yb-ETTC, Yb-BCPP, and Yb-CTTB were 2.64 eV, 3.34 eV, 3.86 eV, and 3.77 eV, respectively. Among all Yb-MOFs, Yb-TCPP had the lowest HOMO-LUMO energy gap, and thus could better promote electron capture in electrochemical processes, resulting in higher ECL intensity of Yb-TCPP.

To build an electrochemical sensor, we modified AuNPs on the surface of the MOFs, enabling them to act as bridges between ECL materials and DNA strands. The AuNPs also improved the electrical conductivity of the material and enhanced the ECL intensity. Stability is an important index for assessing the properties of the material. Therefore, through several cycles of continuous scanning, we found that the ECL intensity of Yb-TCPP@AuNPs had an RSD of 0.37 % (Fig. 2D), which was lower than H_2TCPP (Fig. S9). This indicates that Yb-TCPP@AuNPs have good stability. In addition, compared to that of H_2TCPP, the ECL intensity of Yb-TCPP@AuNPs was stronger, suggesting that the structure of MOF could reduce the ACQ effect. In addition, when the ECL efficiency (Φ_{ECL}) of the $[Ru(bpy)_3]^{2+}$/TEA system is 1, Yb-TCPP@AuNPs exhibited a high Φ_{ECL} of 11 % (Details can be found in Supplementary Material). These comparisons demonstrated that Yb-TCPP@AuNPs had strong and stable ECL properties. As shown in Fig. S10, we further examined the ECL behavior (including the ECL triggering potential and peak potential) of Yb-TCPP@AuNPs/GCE in PBS solution (0.1 M, pH 7.4) containing TEA (35 mM). First of all, the ECL intensity-potential curve of Yb-TCPP@AuNPs/GCE was collected under the potential scanning from −1 V to + 0.65 V, a PMT of 650 V, and an amplifier series of 4 to obtain the complete ECL peak and triggering potential. Yb-TCPP@AuNPs/GCE exhibited a triggering potential of + 0.47 V, and the maximum ECL emission was observed at + 0.57 V. This indicates that Yb-TCPP@AuNPs had a lower excitation potential, which could reduce electrochemical interference and prevent side reactions such as oxygen evolution (1.72 V vs. RHE in Fig. S11).

3.3. Mechanism of Yb-TCPP@AuNPs ECL system

We carried out ECL and cyclic voltammetry (CV) experiments to verify the ECL mechanism of Yb-TCPP@AuNPs. As shown in Fig. 3A and 3B, the ECL signal detected by modified GCE in PBS solution (Fig. 3A, curve a) and by bare electrode in PBS solution containing TEA (Fig. 3A, curve b) were very low. The corresponding currents were also very low

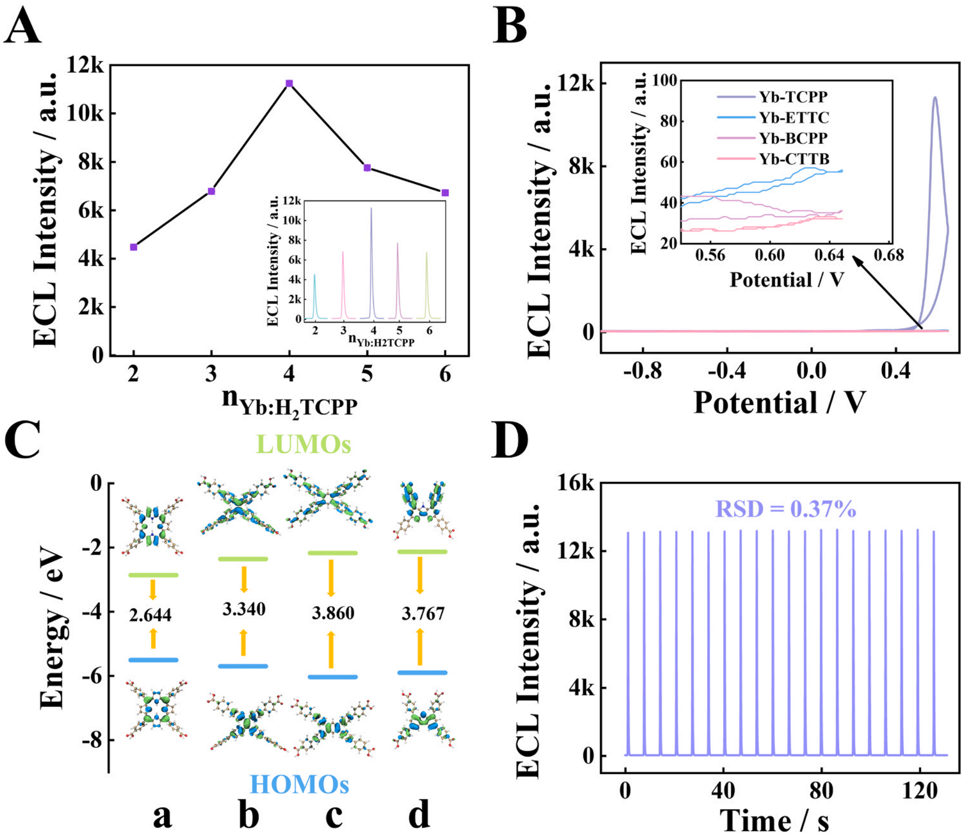

Fig. 2. (A) ECL intensity of Yb-TCPP prepared from Yb and H_2TCPP at different molar ratios. (B) ECL intensity of Yb-TCPP, Yb-ETTC, Yb-BCPP, and Yb-CTTB. (C) Molecular orbitals iso-surface plots and their corresponding energy levels: (a) Yb-TCPP, (b) Yb-ETTC, (c) Yb-BCPP, and (d) Yb-CTTB. (D) Stability of Yb-TCPP@AuNPs during 20 cycles of continuous scanning.

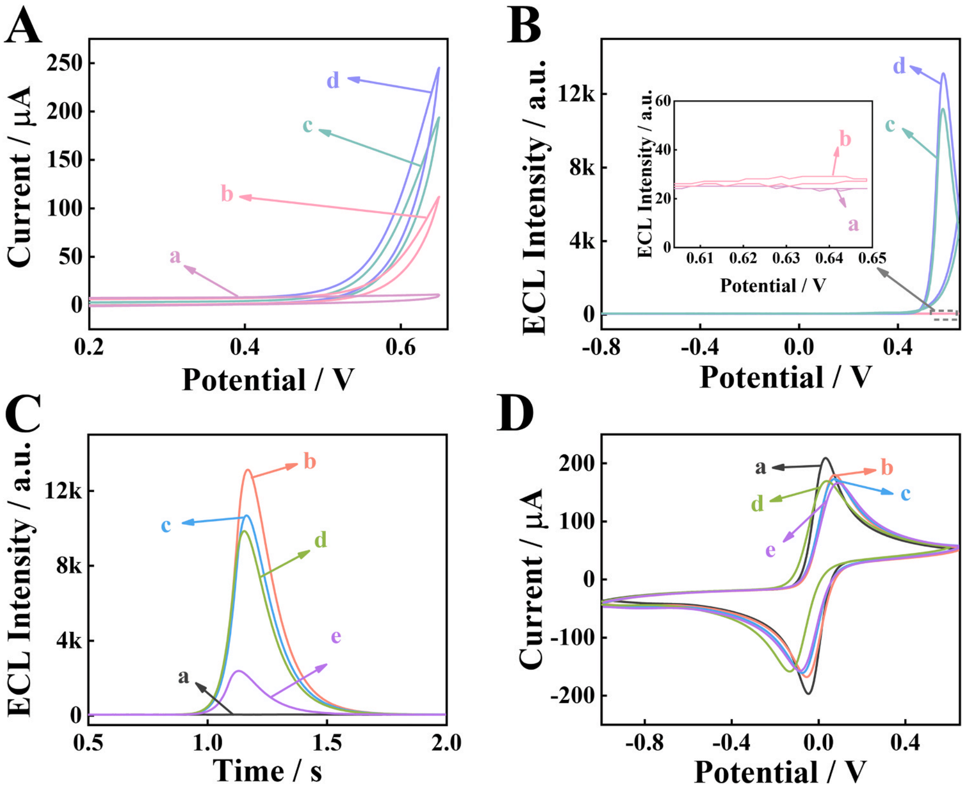

Fig. 3. (A) CV curves and (B) ECL-potential profiles of the various electrodes: Yb-TCPP@AuNPs in PBS solution (0.1 M pH 7.4) (curve a); rare GCE in PBS solution (0.1 M pH 7.4) containing TEA (35 mM) (curve b); Yb-TCPP in PBS solution (0.1 M pH 7.4) containing TEA (35 mM); and Yb-TCPP@AuNPs in PBS solution (0.1 M pH 7.4) containing TEA (35 mM) (curve d). (C) ECL intensity-potential curves of the biosensor during each assembly step: (a) bare GCE; (b) Yb-TCPP@AuNPs/GCE; (c) Y-shaped DNA/Yb-TCPP@AuNPs/GCE; (d) HT/Y-shaped DNA/Yb-TCPP@AuNPs/GCE; and (e) R2/HT/Y-shaped DNA/Yb-TCPP@AuNPs/GCE. (D) CV curves measured in [Fe $(CN)_6]^{3-/4-}$ solution: (a) bare GCE; (b) Yb-TCPP@AuNPs/GCE; (c) Y-shaped DNA/Yb-TCPP@AuNPs/GCE; (d) HT/Y-shaped DNA/Yb-TCPP@AuNPs/GCE; and (e) R2/HT/Y-shaped DNA/Yb-TCPP@AuNPs/GCE.

(Fig. 3B, curves a and b). In the PBS solution containing TEA, the ECL signal (Fig. 3A, curve c) and the current (Fig. 3B, curve c) of Yb-TCPP-modified GCE were significantly increased. After modification with AuNPs, the ECL intensity (Fig. 3B, curve d) and current (Fig. 3A, curve d) were further increased, demonstrating that AuNPs improved the electron transport rate. The entire process is similar to the mechanism of [Ru $(bpy)_3]^{2+}$ and tripropylamine (TPrA) [37]. That is, TEA loses its electrons to form a strong reducing agent, $TEA^{\bullet}$. Then, $TEA^{\bullet}$ reacts with the oxidation state of Yb-TCPP@AuNPs^{+} to form the excited state Yb-TCPP@AuNPs*. Finally, Yb-TCPP@AuNPs* returns to its ground state and generates strong ECL emission. The possible ECL reaction mechanisms of Yb-TCPP@AuNPs are as follows:

$$[\text{Yb-TCPP@AuNPs}] - e^- \rightarrow [\text{Yb-TCPP@AuNPs}]^{+} \quad (1)$$

$$\text{TEA} - e^- \rightarrow \text{TEA}^{\bullet} + H^{+} \quad (2)$$

$$\text{TEA}^{\bullet} + [\text{Yb-TCPP@AuNPs}]^{+} \rightarrow [\text{Yb-TCPP@AuNPs}]^{*} \quad (3)$$

$$[\text{Yb-TCPP@AuNPs}]^{*} \rightarrow [\text{Yb-TCPP@AuNPs}] + h\nu \quad (4)$$

3.4. Characterization of modified ECL biosensor

To verify the feasibility in detection of the constructed ECL biosensor, we characterized its assembly process. First, the ECL intensity versus time curve was verified. As shown in Fig. 3C, the bare electrode did not exhibit a signal (curve a). Conversely, the signal was significantly enhanced when the electrode was modified with Yb-TCPP@AuNPs (curve b). When the Y-shaped DNA structure (0.2 μM) (curve c) and HT (1 μM) (curve d) were sequentially modified on Yb-TCPP@AuNPs, the signal was slightly reduced. When R2 (1 μM) containing ferrocene hybridized with the Y-shaped DNA structure, the signal plummeted (curve e). In addition, CV and electrochemical impedance spectroscopy (EIS) were further used to verify the modified biosensor. As shown in Figs. 3D and S12, after Yb-TCPP@AuNPs was modified on the bare electrode, both the current and impedance changed significantly (curve b) compared to the bare GCE (curve a). After the Y-shaped DNA structure (curve c) and HT (curve d) were modified, the current decreased, and correspondingly, the diameter of the semicircle impedance increased. This is likely due to the electrostatic repulsion between the negatively charged DNA and [Fe $(CN)_6]^{3-/4-}$, as well as the blocking effect of HT on the electrons [38]. When R2 containing ferrocene hybridized with the Y-shaped DNA structure (curve e), the redox peak current decreased, and the impedance semicircle diameter increased. All in all, the above characterization shows that the sensor was successfully assembled (Scheme 1).

3.5. Optimization of reaction conditions

To find the optimal conditions, we optimized the reaction conditions. As shown in Fig. 4A and Fig. S13, Yb-TCPP@AuNPs exhibited a strong ECL signal at pH 7. This is due to the pKa value (acid dissociation constant) for the deprotonation of the tertiary amine group in the co-reactant molecules, which affects the ECL profiles verses the electrolyte pH [39,40]. In order to achieve better quenching, we optimized the incubation time and concentration of R2 containing ferrocene. As shown in Figs. 4B and 4D, when the incubation time of R2 containing ferrocene was 2 h, the ECL signal was the lowest and tended to be stable. Additionally, when the concentration of R2 containing ferrocene was 1 μM, a better quenching effect was achieved. We also optimized the shearing

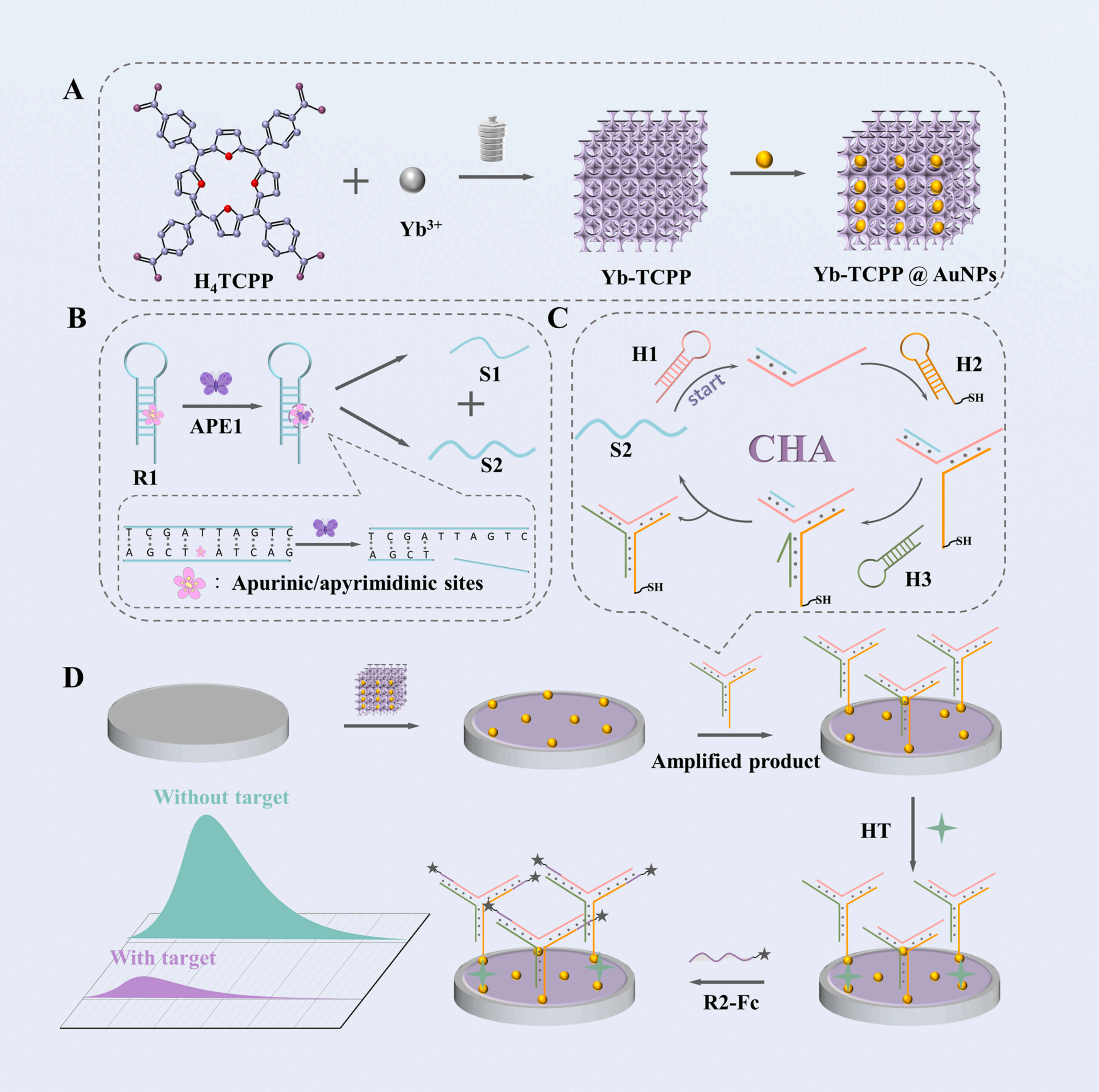

Scheme 1. Illustration of the designed ECL biosensor in the sensitive detection of target APE1. (A) Synthesis of Yb-TCPP@AuNPs. (B) Shear process of APE1. (C) S2-triggered CHA amplification circuit. (D) Assembly process of ECL biosensor.

time of APE1. As shown in Fig. 4C, the ECL signal changed smoothly after 60 min, indicating that the shearing at the AP sites could be completed within 60 min. In Fig. S13, the optimal concentration of the Y-shaped DNA was 0.2 μM. The insufficient concentration of Y-shaped DNA can lead to reduced hybridization efficiency with S2-Fc, resulting in an unsatisfactory quenching effect. Conversely, excessively high concentrations of Y-shaped DNA will cause significant quenching, which will affect the subsequent linear detection signal change being not obvious. In summary, the optimal test conditions based on multiple factors were as follows: pH of 7.4, incubation time of 2 h, ferrocene quenching concentration of 1 μM, APE1 shearing time of 1 h, and Y-shaped DNA concentration of 0.2 μM.

3.6. Performances of the proposed ECL biosensor

We evaluated the quantitative analytical-performance of the ECL sensor in detecting APE1 under optimal conditions. As shown in Fig. 5A and B, the ECL intensity gradually decreased with increasing APE1 concentration (10^{-8} - 10^{-2} U/mL). As illustrated in Fig. 5C, the ECL intensity was negatively correlated with the logarithmic value of APE1 concentration (log c). The linear equation was: I_{ECL} = -954.13 log c + 731.58, with a correlation coefficient of 0.9989. The limit of detection (LOD) was 1.58×10^{-9} U/mL at a signal-to-noise ratio (S/N) of 3 (Fig. S14). Compared to other strategies reported in the literature, our proposed ECL biosensor was more sensitive and had higher performance and lower LOD in detecting APE1. Table S3 lists a comparison between the proposed biosensor in this study and other APE1 detection methods

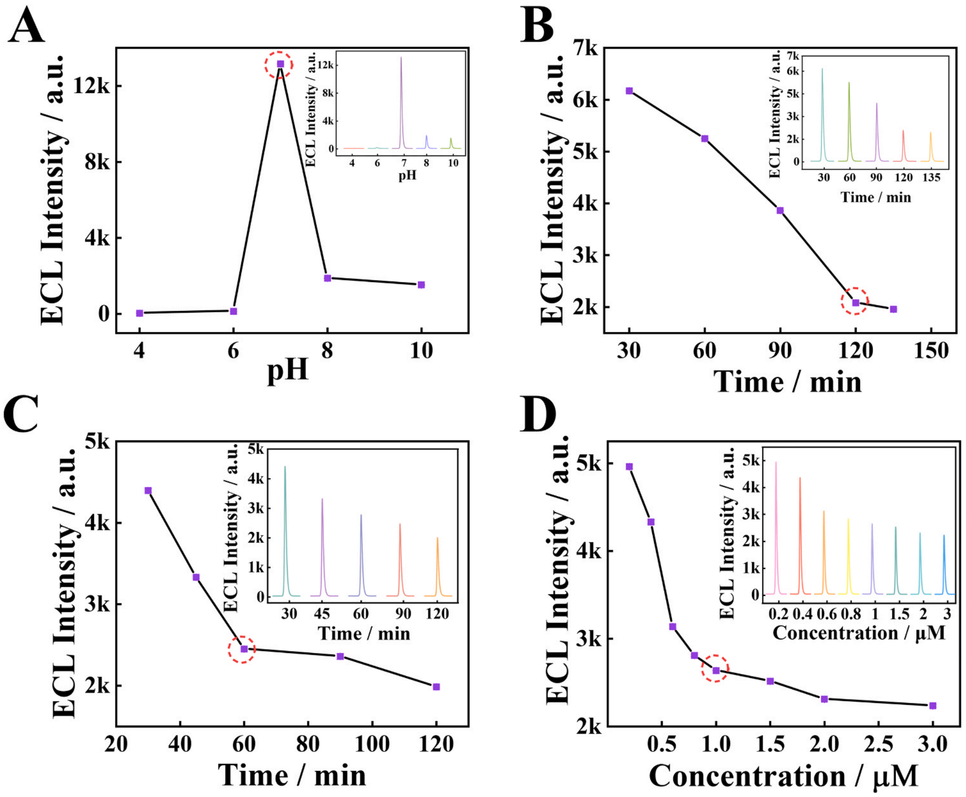

Fig. 4. Optimizations of (A) pH of PBS solution (0.1 M), (B) incubation time of R2 with ferrocene, (C) reaction time of R1 and APE1, and (D) concentration of R2 containing ferrocene.

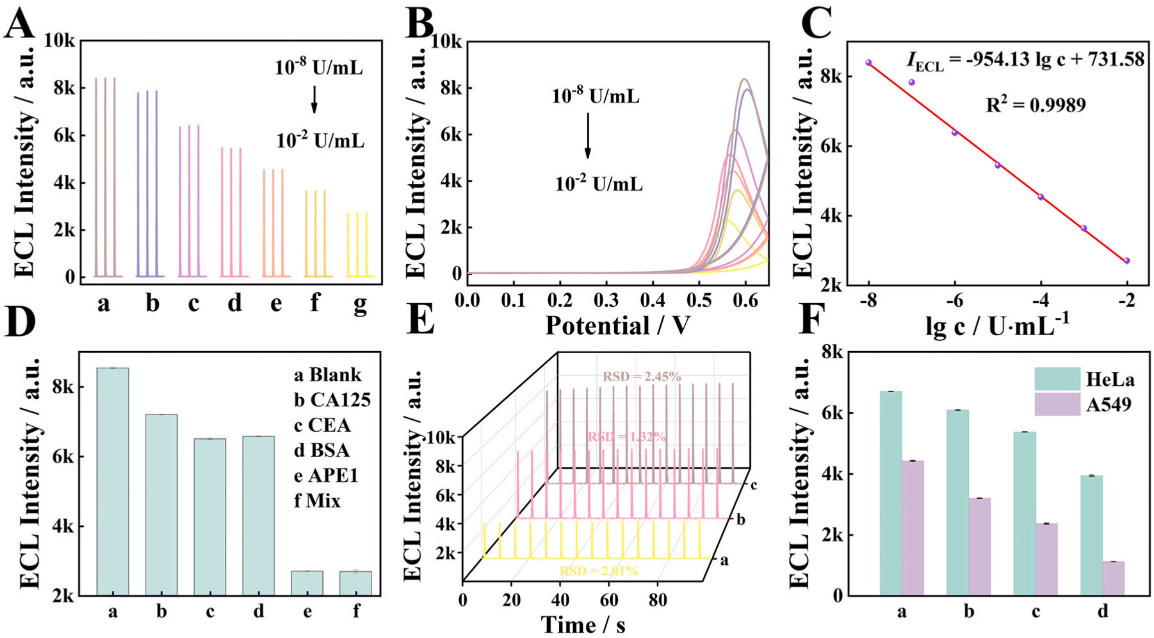

Fig. 5. (A) ECL responses of the proposed biosensor in the presence of APE1 at different concentrations from 1 × 10^{-8} U/mL to 1 × 10^{-2} U/mL (curves a-g). (B) ECL intensity-potential curves of the biosensor incubated with APE1 at different concentrations. (C) Linear curve of ECL intensity versus the logarithm of APE1 concentration (n = 3). (D) Selectivity of the biosensor to a blank sample, APE1 (10^{-2} U/mL) alone, 0.1 mg/mL interfering substances (CA125, CEA, and BSA), and their mixtures in 0.1 M PBS solution (pH 7.4) containing 35 mM TEA. Scanning range: −1.0 V - + 0.65 V. Scanning rate: 500 mV·s^{-1}. (E) Stability of ECL intensity of 1 × 10^{-2} U/mL APE1 (a), 1 × 10^{-5} U/mL APE1 (b), and 1 × 10^{-8} U/mL APE1 (c) during 15 scans. (F) ECL intensity of the biosensor during the detection of APE1 in different cells (HeLa and A549) at varying amounts: (a) 1 × 10^2, (b) 1 × 10^3, (c) 1 × 10^4, and (d) 1 × 10^5 cells.

reported in the literature.

3.7. Stability and selectivity of the proposed ECL biosensor

To further evaluate the selectivity of the biosensor, we used CA125, CEA, and BSA as disruptors in a comparative experiment. As shown in Fig. 5D, when other cancer markers (CA125, CEA, and BSA) at a concentration of 0.1 mg/mL were used as the target, the decrease in ECL intensity was not significant. However, the signal was significantly reduced in the presence of APE1. When the three interferents were mixed with the target APE1, the ECL intensity was approximately the same as that of APE1 alone. This shows that the ECL sensor has good selectivity.

In order to evaluate the stability of the biosensor, we took 1×10^{-2} U/mL, 1×10^{-5} U/mL and 1×10^{-8} U/mL APE1 as an example and continuously scanned the biosensor for 15 cycles. As shown in Fig. 5E, the RSD were 2.01 %, 1.32 %, and 2.45 %, indicating that the ECL biosensor has good stability.

3.8. Application of the biosensor in real samples

According to the standard addition method, we examined the ECL signal of APE1 at different concentrations (1×10^{-3} U/mL, 1×10^{-5} U/mL, and 1×10^{-7} U/mL) in normal serum diluted 1000 times. We then calculated the corresponding concentrations using the standard curve and the ECL intensity. The recovery rates were determined based on the ratio between the calculated result and the standard concentration and were found to be between 95.5 % and 105.0 % (Table S2). These results demonstrate that the proposed ECL biosensor can detect APE1 in real human samples and can be applied to the clinical detection of APE1. To further evaluate the suitability of this ECL biosensor for APE1 detection in cell lysates, we selected HeLa and lung cancer cells (A549 cells). As shown in Fig. 5 F, when the number of A549 cells was increased from 1×10^{2} to 1×10^{5} cells, the ECL signal gradually decreased. In contrast, when the number of HeLa cells was increased from 1×10^{2} to 1×10^{5} cells, the ECL signal decreased very slowly, at a slower rate than A549 cells. These results show that the expression level of APE1 in A549 cells is higher than that in HeLa cells, which is consistent with previous reports [41].

4. Conclusions

In summary, we successfully developed Yb-TCPP@AuNPs as a novel anodic ECL material with strong and stable ECL emission. The material was synthesized via hydrothermal reaction and further modified with AuNPs to enhance its electrical conductivity and ECL performance. Yb-TCPP@AuNPs had a low triggering potential (+0.47 V) and thus could effectively prevent oxygen evolution side reactions. They also had excellent ECL efficiency and stability, thus representing a promising platform for advanced biosensing applications. As a proof of concept, we constructed an "on-off" ECL biosensor for APE1 detection. The biosensor had excellent selectivity and stability and was successfully applied to detect APE1 in lung cancer cells and real human serum samples. Overall, this work presents a new idea for exploring efficient ECL materials and a new strategy for the rapid and accurate detection of the cancer marker APE1.

CRediT authorship contribution statement

Wu Qiong: Resources, Investigation. **Song Daqian:** Supervision, Resources, Project administration, Funding acquisition. **Ma Pinyi:** Writing – review & editing, Project administration, Data curation, Conceptualization. **Zhang Yan:** Methodology, Investigation. **Ma Mo:** Investigation, Formal analysis. **Ye Zhuoxin:** Validation, Investigation, Formal analysis. **Chen Yuxuan:** Investigation, Data curation. **Liu Ruiyan:** Writing – original draft, Validation, Investigation, Formal analysis, Data curation, Conceptualization. **Xu Yike:** Investigation, Data curation.

Declaration of Competing Interest

The authors declare that they have no known competing financial interests or personal relationships that could have appeared to influence the work reported in this paper.

Acknowledgements

This work was supported by the National Natural Science Foundation of China (22074052 and 22004046), the Science and Technology Developing Foundation of Jilin Province of China (20230101033JC), Jilin Provincial Department of Education Program for Enhancing Ph.D. Students' Scientific Research and Innovation Capabilities (JJKH20250064BS), and Jilin Provincial College Student Innovation and Entrepreneurship Training Program (S202310183632).

Appendix A. Supporting information

Supplementary data associated with this article can be found in the online version at doi:10.1016/j.snb.2025.137687.

Data availability

Data will be made available on request.

References

[1] L. Li, Y. Chen, J.-J. Zhu, Recent advances in electrochemiluminescence analysis, Anal. Chem. 89 (2016) 358–371.

[2] X. Yang, Y. Xu, X. Huang, J. Hang, W. Guo, Z. Dai, Multicolor iridium(III) complexes with host-guest recognition motifs for enhanced electrochemiluminescence and modular labeling, Anal. Chem. 95 (2023) 4543–4549.

[3] Y. Chen, Z. Ye, M. Ma, J. Yang, R. Liu, Y. Zhang, et al., Electrochemiluminescence biosensor for specific detection of pancreatic ductal carcinoma through dual targeting of MUC1 and miRNA-196a, Biosens. Bioelectron. 254 (2024) 116241.

[4] C. Li, S. Wang, Y. Huang, B. Zheng, Z. Tian, Y. Wen, et al., Synthesis, characterization and electrochemiluminescent properties of cyclometalated platinum(II) complexes with substituted 2-phenylpyridine ligands, Dalton Trans. 42 (2013) 4059–4067.

[5] J.L. Liu, Z.L. Tang, J.Q. Zhang, Y.Q. Chai, Y. Zhuo, R. Yuan, Morphology-controlled 9,10-diphenylanthracene nanoblocks as electrochemiluminescence emitters for microRNA detection with one-step DNA walker amplification, Anal. Chem. 90 (2018) 5298–5305.

[6] Q. Li, Z. Wang, M. Xu, J. Li, Y. Li, D. Hua, Visualized electrochemiluminescence iodine sensor based on polymer dots with Co-reactive group for real-time monitoring system, Talanta 257 (2023) 124369.

[7] Z. Ye, Y. Liu, M. Pan, X. Tao, Y. Chen, P. Ma, et al., AgInZnS quantum dots as anodic emitters with strong and stable electrochemiluminescence for biosensing application, Biosens. Bioelectron. 228 (2023) 115219.

[8] Y.M. Lei, M. Zhao, A. Wang, Y.Q. Yu, Y.Q. Chai, R. Yuan, et al., Electrochemiluminescence of supramolecular nanorods and their application in the "On-Off-On" detection of copper ions, Chem. Eur. J. 22 (2016) 8207–8214.

[9] Y.X. Li, J. Li, W.R. Cai, W.L. Xin, R.S. Marks, H.B. Zeng, et al., Postsynthesis ligand exchange induced porphyrin hybrid crystalloid reconstruction for self-enhanced electrochemiluminescence, Anal. Chem. 92 (2020) 15270–15274.

[10] G. Liu, J. Hong, K. Ma, Y. Wan, X. Zhang, Y. Huang, et al., Porphyrin trio-pendant fullerene guest as an In situ universal probe of high ECL efficiency for sensitive miRNA detection, Biosens. Bioelectron. 150 (2020) 111963.

[11] I. Stassen, N. Burtch, A. Talin, P. Falcaro, M. Allendorf, R. Ameloot, An updated roadmap for the integration of metal-organic frameworks with electronic devices and chemical sensors, Chem. Soc. Rev. 46 (2017) 3185–3241.

[12] D. Bhatt, S. Singh, N. Singhal, N. Bhardwaj, A. Deep, Glyco-conjugated metal-organic framework biosensor for fluorescent detection of bacteria, Anal. Bioanal. Chem. 415 (2023) 659–667.

[13] Y. Wang, J. Shu, A. Lyu, M. Wang, C. Hu, H. Cui, Zn^{2+}-modified nonmetal porphyrin-based metal-organic frameworks with improved electrochemiluminescence for nanoscale exosome detection, ACS Appl. Nano Mater. 6 (2023) 4214–4223.

[14] L. Zhao, X. Ren, Y. Du, Z. Gao, H. Ma, H. Wang, et al., Europium-based metal-organic framework with N—H···π interaction and intramolecular energy transfer mechanisms for self-electrochemiluminescence, Adv. Funct. Mater. 34 (2024) 2410886.

[15] L. Zhao, X. Song, X. Ren, D. Fan, Q. Wei, D. Wu, Rare self-luminous mixed-valence Eu-MOF with a self-enhanced characteristic as a near-infrared fluorescent ecl probe for nondestructive immunodetection, Anal. Chem. 93 (2021) 8613–8621.

[16] L. Zhao, X. Song, X. Ren, H. Wang, D. Fan, D. Wu, et al., Ultrasensitive near-infrared electrochemiluminescence biosensor derived from Eu-MOF with antenna effect and high efficiency catalysis of specific CoS_2 hollow triple shelled nanoboxes for procalcitonin, Biosens. Bioelectron. 191 (2021) 113409.

[17] B. Wang, L. Zhao, Y. Li, X. Liu, D. Fan, D. Wu, et al., Porphyrin-based metal-organic frameworks enhanced electrochemiluminescence (ECL) by overcoming aggregation-caused quenching: a new ECL emitter for the detection of trenbolone, Anal. Chim. Acta 1276 (2023) 341616.

[18] P.B. Siqueira, M.M. de Sousa Rodrigues, Í.S.S. de Amorim, T.G. da Silva, M. da Silva Oliveira, J.A. Rodrigues, et al., The APE1/REF-1 and the hallmarks of cancer, Mol. Biol. Rep. 51 (2024) 47.

[19] G. Antoniali, E. Dalla, G. Mangiapane, X. Zhao, X. Jing, Y. Cheng, et al., APE1 controls DICER1 expression in NSCLC through miR-33a and miR-130b, Cell. Mol. Life Sci. 79 (2022) 446.

[20] G. Mangiapane, D. Pascut, E. Dalla, G. Antoniali, M. Degrassi, L.S. Crocè, et al., Clinical significance of apurinic/apyrimidinic endodeoxyribonuclease 1 and microrna axis in hepatocellular carcinoma, J. Clin. Transl. Hepatol. 11 (2023) 1291–1307.

[21] E. Coskun, P. Jaruga, P.T. Reddy, M. Dizdaroglu, Extreme expression of DNA repair protein apurinic/apyrimidinic endonuclease 1 (APE1) in human breast cancer as measured by liquid chromatography and isotope dilution tandem mass spectrometry, Biochemistry 54 (2015) 5787–5790.

[22] A. Sharma, P. Verwilst, M. Li, D. Ma, N. Singh, J. Yoo, et al., Theranostic fluorescent probes, Chem. Rev. 124 (2024) 2699–2804.

[23] W. Zhang, L. Chen, K. Yang, L. Wang, B. Han, S. Sun, et al., An electrochemiluminescence immunosensor based on functionalized metal organic layers as emitters for sensitive detection of carcinoembryonic antigen, Sens. Actuators B Chem. 393 (2023) 134317.

[24] W. Zhang, D. Han, Z. Wu, K. Yang, S. Sun, J. Wen, Metal-organic layers-catalyzed amplification of electrochemiluminescence signal and its application for immunosensor construction, Sens. Actuators B Chem. 376 (2023) 133004.

[25] Z.W. Jiang, Y.C. Zou, T.T. Zhao, S.J. Zhen, Y.F. Li, C.Z. Huang, Controllable synthesis of porphyrin-based 2D lanthanide metal-organic frameworks with thickness- and metal-node-dependent photocatalytic performance, Angew. Chem. Int. Ed. 59 (2020) 3300–3306.

[26] P.-H. Tong, J.-J. Wang, X.-L. Hu, T.D. James, X.-P. He, Metal-organic framework (MOF) hybridized gold nanoparticles as a bifunctional nanozyme for glucose sensing, Chem. Sci. 14 (2023) 7762–7769.

[27] Z.W. Jiang, T.T. Zhao, S.J. Zhen, C.M. Li, Y.F. Li, C.Z. Huang, A 2D MOF-based artificial light-harvesting system with chloroplast bionic structure for photochemical catalysis, J. Mater. Chem. A 9 (2021) 9301–9306.

[28] Z.W. Jiang, T.T. Zhao, C.M. Li, Y.F. Li, C.Z. Huang, 2D MOF-based photoelectrochemical aptasensor for SARS-CoV-2 spike glycoprotein detection, ACS Appl. Mater. Interfaces 13 (2021) 49754–49761.

[29] Z. Wei, Z.Y. Gu, R.K. Arvapally, Y.P. Chen, R.N. McDougald Jr., J.F. Ivy, et al., Rigidifying fluorescent linkers by metal-organic framework formation for fluorescence blue shift and quantum yield enhancement, J. Am. Chem. Soc. 136 (2014) 8269–8276.

[30] Z. Hu, G. Huang, W.P. Lustig, F. Wang, H. Wang, S.J. Teat, et al., Achieving exceptionally high luminescence quantum efficiency by immobilizing an AIE molecular chromophore into a metal-organic framework, Chem. Commun. 51 (2015) 3045–3048.

[31] J. Pang, S. Yuan, J. Qin, M. Wu, C.T. Lollar, J. Li, et al., Enhancing pore-environment complexity using a trapezoidal linker: toward stepwise assembly of multivariate quinary metal-organic frameworks, J. Am. Chem. Soc. 140 (2018) 12328–12332.

[32] W.C. Hu, M.R. Younis, Y. Zhou, C. Wang, X.H. Xia, In situ fabrication of ultrasmall gold nanoparticles/2D MOFs hybrid as nanozyme for antibacterial therapy, Small 16 (2020) 2000553.

[33] C. Wang, Z. Li, H. Ju, Copper-doped terbium luminescent metal organic framework as an emitter and a co-reaction promoter for amplified electrochemiluminescence immunoassay, Anal. Chem. 93 (2021) 14878–14884.

[34] A. Fiorani, G. Valenti, M. Iurlo, M. Marcaccio, F. Paolucci, Electrogenerated chemiluminescence: a molecular electrochemistry point of view, Curr. Opin. Electrochem 8 (2018) 31–38.

[35] K.I. Williamson, D.J.C. Herr, Y. Mo, Mapping the correlations between bandgap, HOMO, and LUMO trends for meta substituted Zn-MOFs, J. Comput. Chem. 45 (2024) 2119–2127.

[36] M. Shao, Y. Li, M. Chen, W. Liu, Y. Sun, Y. Chu, et al., High-efficiency electrogenerated chemiluminescence of novel zr-based metal-organic frameworks through organic linkers regulation, ChemElectroChem 9 (2022) e202200866.

[37] Y. Yuan, S. Han, L. Hu, S. Parveen, G. Xu, Coreactants of tris(2,2′-bipyridyl) ruthenium(II) electrogenerated chemiluminescence, Electrochim. Acta 82 (2012) 484–492.

[38] J.-L. Liu, Z.-L. Tang, Y. Zhuo, Y.-Q. Chai, R. Yuan, Ternary electrochemiluminescence system based on rubrene microrods as luminophore and Pt nanomaterials as coreaction accelerator for ultrasensitive detection of microrna from cancer cells, Anal. Chem. 89 (2017) 9108–9115.

[39] X.B. Yin, B.B. Sha, X.H. Zhang, X.W. He, H. Xie, The factors affecting the electrochemiluminescence of tris(2,2′-bipyridyl)Ruthenium(II)/TErtiary Amines, Electroanalysis 20 (2008) 1085–1091.

[40] N. Govindarajan, A. Xu, K. Chan, How pH affects electrochemical processes, Science 375 (2022) 379–380.

[41] K. Long, L. Gu, L. Li, Z. Zhang, E. Li, Y. Zhang, et al., Small-molecule inhibition of APE1 induces apoptosis, pyroptosis, and necroptosis in non-small cell lung cancer, Cell Death Dis. 12 (2021) 503.

Ruiyan Liu is currently a master degree student in College of Chemistry, Jilin University. Her research interest is electrochemical biosensor.

Yike Xu is currently an undergraduate in The Third Bethune Hospital of Jilin University. Her interest is electrochemical biosensor.

Zhuoxin Ye is currently a Ph.D. student in College of Chemistry, Jilin University. Her research interest is electrochemical biosensor.

Yuxuan Chen is currently a master degree student in College of Chemistry, Jilin University. Her research interest is electrochemical biosensor.

Yan Zhang is currently a master degree student in College of Chemistry, Jilin University. Her research interest is electrochemical biosensor.

Mo Ma is currently a Ph.D. student in School of Pharmacy, Jilin University. His research interest is spectral analysis.

Pinyi Ma received his doctor's degree from College of Chemistry, Jilin University in 2017 and he is an associate professor in that school. His research area is spectral analysis.

Qiong Wu gained her doctor's degree from College of Chemistry, Jilin University in 2018 and she is an associate professor in China-Japan Union Hospital of Jilin University. Her research area is spectral analysis and biosensor.

Daqian Song received his doctor's degree from College of Chemistry, Jilin University in 2003 and he is a professor in that school. His research areas are spectral and chromatography analysis.